Quantum Transport in Bismuth Two-Dimensional Electron System

Di Yue,[1,2,3,4,5,*] Hongya Wang,[1,2,3,4,5,*] Guangyi Huang,[1,*] Yadong Jiang,[1] Zhiwei Huang,[1,2,3,4,5] Pengyu Zheng,[1,2,3,4,5] Yichen Song,[1,2,3,4,5] Shuaifei Guo,[1,2,3,4,5] Ning Tian,[1,2,3,4,5] Mingyan Luo,[1,2,3,4,5] Zhongxun Guo,[1,2,3,4,5] Hengsheng Luo,[1,2,3,4,5] Chuanying Xi,[6] Guangli Kuang,[6] Kenji Watanabe,[7] Takashi Taniguchi,[8] Zhimou Chen,[9] Xi Lin,[9] Jing Wang,[1,2,†] Changlin Zheng,[1,‡] Xiaofeng Jin,[1] Wei Ruan,[1,2,3,4,5,§] and Yuanbo Zhang[1,2,3,4,5,10,‖]

[1]*State Key Laboratory of Surface Physics and Department of Physics, Fudan University, Shanghai 200438, China*
[2]*Institute for Nanoelectronic Devices and Quantum Computing, Fudan University, Shanghai 200433, China*
[3]*Shanghai Branch, Hefei National Laboratory, Shanghai 201315, China*
[4]*Shanghai Research Center for Quantum Sciences, Shanghai 201315, China*
[5]*Zhangjiang Fudan International Innovation Center, Fudan University, Shanghai 201210, China*
[6]*Anhui Province Key Laboratory of Condensed Matter Physics at Extreme Conditions, High Magnetic Field Laboratory, HFIPS, Chinese Academy of Sciences, Hefei 230031, China*
[7]*Research Center for Electronic and Optical Materials, National Institute for Materials Science, 1-1 Namiki, Tsukuba 305-0044, Japan*
[8]*Research Center for Materials Nanoarchitectonics, National Institute for Materials Science, 1-1 Namiki, Tsukuba 305-0044, Japan*
[9]*International Center for Quantum Materials, Peking University, Beijing 100871, China*
[10]*New Cornerstone Science Laboratory, Shenzhen 518054, China*

(Received 31 October 2024; revised 12 September 2025; accepted 4 November 2025; published 9 December 2025)

Two-dimensional electron systems (2DESs) have represented an ever-expanding frontier in condensed matter physics. Over the past two decades, this growth has primarily been propelled by the emergence of novel 2DESs, exemplified by graphene and other two-dimensional (2D) crystals, each exhibiting distinctive properties. In this study, we synthesize high-quality β-phase bismuth thin films on exfoliated hexagonal boron nitride (hBN) and establish that bismuth surface states form a high-mobility 2DES with strong spin-orbit coupling (SOC). The extreme two dimensionality of the 2DES is characterized by an out-of-plane to in-plane effective-mass-anisotropy lower bound exceeding 10^3. We further demonstrate that the spin degeneracy of the hole pockets is completely lifted, providing unambiguous transport evidence that they originate from Rashba states induced by strong SOC in the bismuth thin film. Under magnetic fields up to 40 Tesla, electrostatic gating drives the carriers into the lowest Landau levels, revealing signatures of rotational symmetry breaking and electronic nematicity. These findings position the bismuth 2DES as a compelling platform for exploring topological quantum phenomena in systems with strong SOC and high carrier mobility.

DOI: 10.1103/hptx-pw9s

Subject Areas: Condensed Matter Physics, Mesoscopics

I. INTRODUCTION

Bismuth occupies a pivotal role in the formative years of modern condensed matter physics. It was the primary medium for a number of quantum phenomena that later became foundational to the field [1–3]. Notable among these phenomena are diamagnetism [4], the Nernst effect [5], and the Shubnikov–de Haas (SdH) and de Haas–van Alphen effects [6,7]. Much of these pioneering discoveries, viewed from a contemporary perspective, can be attributed to the extraordinary material properties of bismuth. As a quintessential semimetal, bismuth is characterized by an extremely small Fermi surface—approximately 10^{-5} of the Brillouin zone—with nearly balanced electron and hole carriers. This electronic structure results in a low effective

*These authors contributed equally to this work.
†Contact author: wjingphys@fudan.edu.cn
‡Contact author: zcl@fudan.edu.cn
§Contact author: weiruan@fudan.edu.cn
‖Contact author: zhyb@fudan.edu.cn

Published by the American Physical Society under the terms of the Creative Commons Attribution 4.0 International license. Further distribution of this work must maintain attribution to the author(s) and the published article's title, journal citation, and DOI.

mass and a large Fermi wavelength, which together contribute to an unusually long mean free path on the order of micrometers and an exceptionally high mobility of up to 10^7 $cm^2\,V^{-1}\,s^{-1}$ in bulk bismuth. Additionally, bismuth exhibits the strongest spin-orbit coupling (SOC) among all nonradioactive elemental solids, further underscoring its significance in the study of condensed matter [8,9]. Indeed, spectroscopic measurements have indicated that bismuth surface states possess nontrivial topology [10,11] and can host a nematic valley-polarized quantum Hall liquid [12].

While research on bismuth maintained considerable interest over the past century [13–18], the advent of 2D materials has introduced a fresh perspective [19,20]. Novel physics often emerges each time a new member is introduced into the 2DES family [21–38]. Bismuth, recognized as a van der Waals (vdW) layered material made up of stacked rhombohedral layers [39,40], presents an intriguing opportunity. There is significant potential to develop a 2DES that inherits the exceptional properties of rhombohedral β-phase bulk bismuth, such as strong SOC and high mobility, which could significantly impact 2DES research.

However, creating a bismuth-based 2DES has proven to be extremely challenging. Bulk bismuth has so far resisted mechanical exfoliation [41–43], and monolayer bismuth grown on SiC substrates (or on Bi_2Te_3 substrates) is plagued by defects and small domain sizes [44–46] (or by the overlap of band dispersions of bismuth and Bi_2Te_3 [47,48]). Moreover, production of thin-film β-phase bismuth using conventional molecular beam epitaxy (MBE) is hampered by an inevitable amorphous wetting layer, followed by the growth of the orthorhombic α phase; only beyond a critical thickness does the film transition to the rhombohedral β phase [49–53]. Recently, a hot-pressing technique has been developed to produce ultrathin bismuth films [54–56]. Notably, Chen *et al.* achieved sub-10-nm-thick bismuth layers by squeezing molten bismuth between two hBN flakes, yielding β-phase films that exhibit exceptional transport properties, including multicarrier quantum oscillations tunable by electrostatic gating [55].

Here, we report the bottom-up synthesis of high-quality bismuth ultrathin films using vdW epitaxy [57] on exfoliated hBN. The small lattice mismatch (around 4.6%), combined with the atomically flat surface of hBN [27], allows us to grow single-crystal β-phase bismuth films as thin as around 2.5 nm. More importantly, we demonstrate that the bismuth surface states [39,58–64] at the bismuth/hBN interface forms a high-mobility 2DES with strong SOC. The extreme 2D nature of the 2DES is evidenced by a lower bound on the out-of-plane to in-plane effective mass anisotropy exceeding 10^3, consistent with our calculations showing that the surface states are confined within around 0.8 nm of the film surface. Meanwhile, a detailed analysis of the Landau level (LL) structure of the hole carriers reveals a complete lifting of spin degeneracy, providing direct transport evidence that they originate from Rashba surface states induced by strong SOC. Under strong magnetic fields of up to 40 T, electrostatic gating drives both the electron and hole carriers in bismuth 2DES into the lowest few LLs. In this extreme quantum limit, we resolve the splitting of each initially sixfold-degenerate hole LL, providing clear transport evidence of the rotational symmetry breaking among the six oblong hole pockets—an effect likely arising from strain or electronic nematicity, as previously suggested in scanning tunneling microscopy (STM) studies of the bulk Bi(111) surface [12]. These findings establish the Rashba surface state of bismuth as a new member of the 2DES family and represent a significant advance in the pursuit of novel 2D quantum phenomena.

II. SAMPLE FABRICATION AND CHARACTERIZATION

Figures 1(a)–1(c) illustrate the fabrication steps of the Bi/hBN heterostructure, depicted with an actual specimen. The process begins with a thin hBN flake, typically 10–50 nm thick, mechanically exfoliated onto a SiO_2/Si wafer using adhesive tape [Fig. 1(a)]. The hBN substrate is then annealed at 500 °C in a continuous O_2 flow to eliminate any residual adhesive [65,66] before being loaded into an ultrahigh vacuum (UHV) chamber for the vdW epitaxy growth of bismuth. The growth of bismuth occurs at room temperature at a rate of about 2.4 Å per minute until reaching the nominal thickness [Fig. 1(b)]. Following the deposition, the heterostructure undergoes *in situ* annealing at temperatures ranging from 70 °C to 150 °C, a step crucial for enhancing the crystalline quality of the bismuth film [67]. We define metal contacts by evaporating Au (with typical thickness of 70 nm) through a stencil mask aligned with the sample [35]. The degenerately doped Si now serves as a back gate that modulates the charge carrier concentration in the sample [Fig. 1(c)]. Finally, excess bismuth that shorts the electrodes on the SiO_2 is carefully cut off with a sharp tip, ensuring that electronic transport in subsequent measurements occurs solely through the Bi/hBN heterostructure. More details are given in Appendix C 1.

The vdW epitaxy consistently produces high-quality bismuth films with thicknesses ranging from tens of nanometers down to around 4 nm, as characterized by atomic force microscopy (AFM). By further encapsulating the Bi/hBN stack with an additional hBN layer and annealing gently at around 70 °C, we are able to obtain β-phase bismuth films as thin as 2.5 ± 1.1 nm (see Sec. 9, Supplemental Material [68]). Figure 1(d) presents the Raman spectra of four representative bismuth films, along with that of bulk bismuth. All spectra display the characteristic E_g and A_{1g} peaks of β-phase bismuth. These peaks confirm the rhombohedral structure of the films, down to their interface with the hBN substrate, as the Raman probe penetrates the full thickness of the films. We note that the peaks progressively shift to higher wavenumbers—the E_g peak shifts from 70.9 cm^{-1} to 74.5 cm^{-1} and the A_{1g} from 98.3 cm^{-1} to 100.4 cm^{-1}—as the sample thickness reduces

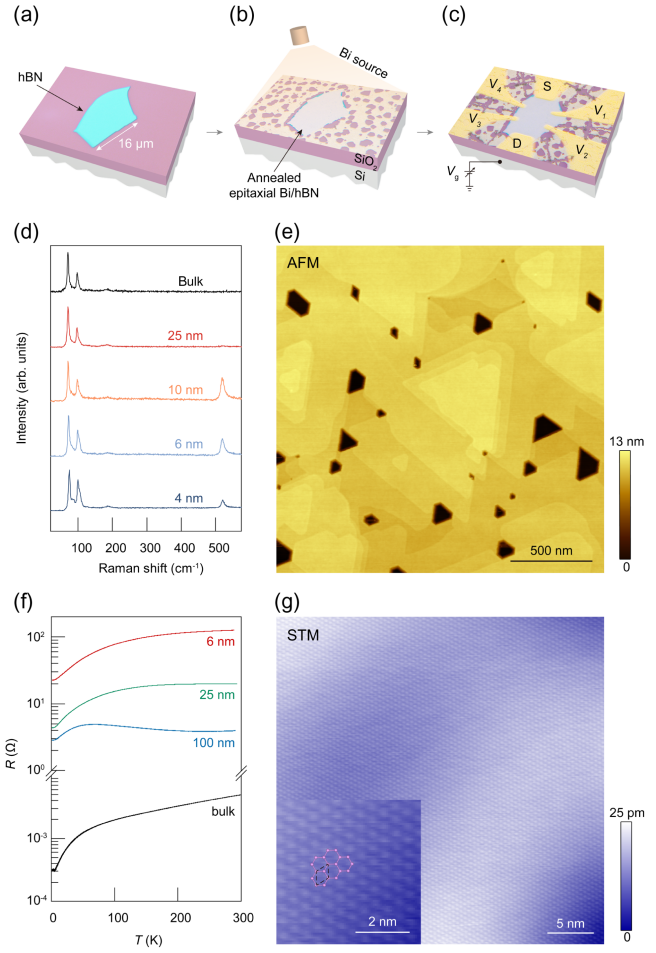


FIG. 1. Fabrication and characterization of the Bi/hBN heterostructure. (a)–(c) Schematic of the device fabrication process illustrated with optical images of an actual sample. The hBN flake (with a thickness of about 40 nm) is mechanically exfoliated onto a Si wafer covered with 285 nm SiO_2 (a), followed by vdW epitaxy growth of bismuth thin films in UHV (b). Multiple Au electrodes (with typical thickness of 70 nm) are then evaporated onto the sample through a stencil mask. (c) Excess bismuth that shorts the electrodes on the SiO_2 is cut off with a sharp tip. A typical transport measurement setup is schematically illustrated in panel (c). The degenerately doped Si now serves as a back gate that modulates the charge carrier concentration in the sample. (d) Raman spectra of the Bi/hBN heterostructure with various bismuth thicknesses. The thickness of the bismuth is marked on each spectrum. The spectrum of bismuth bulk crystal (black) is also shown as a reference. The Raman peak at 520.7 cm^{-1} originates from the Si wafer. (e) AFM image of the top surface of a Bi/hBN heterostructure with nominally 10-nm-thick bismuth. The surface comprises atomic terraces interspersed with pits (see Sec. 1, Supplemental Material [68]). (f) Temperature-dependent sample resistance of Bi/hBN heterostructures with various bismuth thicknesses under zero magnetic field. (g) STM image of the surface of a typical bismuth terrace. The image is obtained at $T = 4.2$ K with a sample bias voltage of $V_s = 100$ mV and a tunneling current $I_s = 6$ nA. Inset: magnified view of the atomically resolved surface with the corresponding bismuth rhombohedral structure model displayed on top.

from 10 ± 1.0 nm to 4 ± 1.4 nm. Meanwhile, an additional peak emerges at 84.0 cm^{-1} in the thinnest samples. These observations suggest slight structural distortions possibly due to strain in the thin films. As shown in Fig. 1(e), AFM of the film's top surface reveals flat terraces approximately 50 nm wide, interspersed with pits approximately 500 nm apart, on average. The terraces, measuring 0.4 nm in height [see Fig. S1(c), Supplemental Material [68]], consist of a single buckled Bi(111) layer. The uniformity in terrace edge orientation, forming 60° or 120° angles, confirms the single crystal domain of the terraces. We find that the domain boundaries are rare; in the collectively examined area of 5.9×10^3 μm^2, only 66 instances were found, indicating large single-crystal domain sizes on the order of around 90 μm^2. Atomically resolved STM imaging of the surface terrace confirms its single-crystal Bi(111) structure [Fig. 1(g)]. Remarkably, no point atomic defects are observed on this 35×35 nm^2 area. Indeed, a typical defect-free area reaches 100×100 nm^2 (Fig. S2), suggesting an areal density of surface point defects below about 10^{10} cm^{-2}.

Of particular interest is the Bi/hBN interface of the heterostructure. We carry out aberration-corrected scanning transmission electron microscopy (STEM) that offers a direct view of this interface with atomic resolution. Details of the STEM measurements are described in Appendix C 2. Figure 2(a) displays a false-color high-angle annular dark field (HAADF) STEM overview of the interface, where the atomically sharp boundary between bismuth and hBN extends along the entire interface. The atomic lattices of both bismuth and hBN become distinctly visible upon closer examination. In particular, STEM imaging along the Bi$[11\bar{2}]$ and Bi$[1\bar{1}0]$ directions [Figs. 2(b) and 2(c)] further confirms the continuous β-phase structure from the interface to the top surface. The high-quality interface is robust against misalignment between the hBN and bismuth lattices—a major advantage of vdW epitaxy [57]. This case is demonstrated in the three high-quality interfaces shown in Figs. 2(b) and 2(c), as well as in Fig. S3; while the Bi $[11\bar{2}]$ direction aligns with hBN [110] of the substrate in Fig. 2(b), the low-Miller-index directions of bismuth and hBN do not match in Figs. 2(c) and S3. Finally, we note that, for bismuth films encapsulated between two hBN flakes, atomically sharp boundaries are consistently observed at both the top and bottom interfaces (see Sec. 4, Supplemental Material [68]).

III. BISMUTH TWO-DIMENSIONAL ELECTRON SYSTEM

Initial insights into surface transport in our Bi/hBN heterostructures come from their temperature-dependent resistance, $R(T)$, presented in Fig. 1(f). As the bismuth thickness decreases to around 100 nm, the $R(T)$ demonstrates a transition from insulating behavior at high temperatures to metallic behavior at lower temperatures [Fig. 1(f), blue curve]. This behavior corroborates the findings in

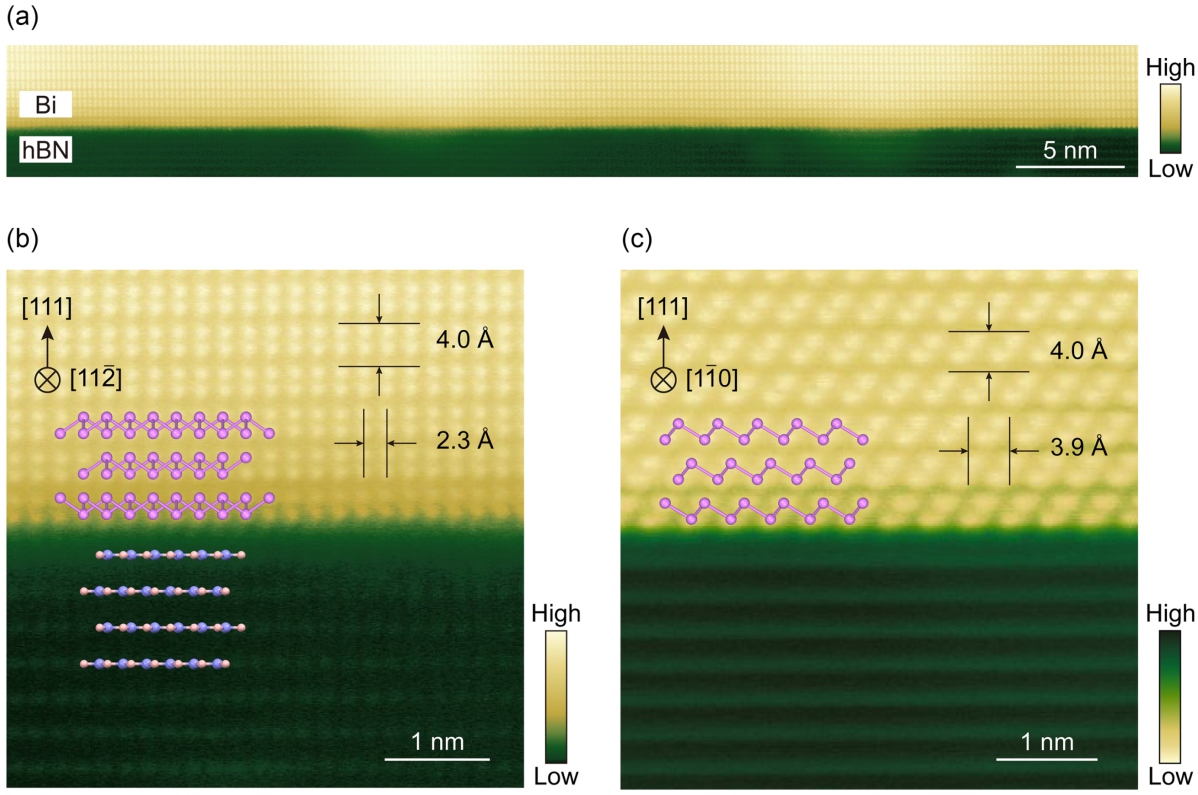


FIG. 2. Cross-sectional STEM characterization of the Bi/hBN interface. (a) False-color HAADF STEM overview of a Bi/hBN interface. The incident electron beam is along the Bi$[11\bar{2}]$ direction (the bisectrix axis). (b) Zoomed-in view of the same Bi/hBN interface as in panel (a). The atomic lattices of both bismuth and hBN are clearly resolved. (c) False-color bright field STEM image of a Bi/hBN interface, with the incident electron beam along the Bi$[1\bar{1}0]$ direction (the binary axis). The structure models of bismuth and hBN are overlaid on top of the STEM images in panels (b) and (c).

Refs. [55,62,63], which attribute the enhanced metallic conduction at low temperatures to predominant surface state contributions. Further reduction in thickness results in a consistent metallic behavior, i.e., surface-dominated conduction, across the entire temperature range.

The surface carriers exhibit high mobility at low temperatures, as evidenced by the quantum oscillations in both R_{yx} and R_{xx} [2,81], which can be tuned via the back gate (see Sec. 5, Supplemental Material [68]). A detailed analysis of these oscillations reveals contributions from two types of carriers—one electronlike and one holelike. Quantitative examination further shows that these carriers originate from the Bi(111) surface states: The electrons stem from the hexagon-shaped electron pocket (EP) near the $\bar{\Gamma}$ point, while the holes arise from six oval-shaped hole pockets (HP) along the $\overline{\Gamma M}$ directions (Fig. S8). These observations are consistent with earlier STM and transport studies [12,55,64]. Full details of the analysis are provided in Secs. 5–9 of the Supplemental Material [68]. Notably, the quantum oscillations onset at a low magnetic field of $B_q \sim 2$ T (Fig. S5), corresponding to a quantum mobility of $\mu_q \sim 1/B_q \sim 5000\ \mathrm{cm^2\,V^{-1}\,s^{-1}}$ [82]. Encapsulating the bismuth layer with a top hBN flake further enhances the quantum mobility to around $10\,000\ \mathrm{cm^2\,V^{-1}\,s^{-1}}$ (Fig. S12)—the highest value reported to date for this system. This exceptional quantum mobility underscores the high quality of the vdW-epitaxy-grown bismuth thin films on hBN.

The high-quality samples enable us to probe the electronic structure of the bismuth surface states with unprecedented precision. In particular, we find that these surface states form a strictly 2DES, as demonstrated by precise mapping of the Fermi surface through analysis of the quantum oscillations in a tilted magnetic field. Since the frequency f of the quantum oscillations measures the extremal cross-sectional area A of the Fermi surface via the Onsager relation $f = (\hbar/2\pi e)A$ [83], a 2DES with a cylindrical Fermi surface exhibits a frequency that scales linearly with $1/\cos\theta$ [84], where θ is the tilt angle [Fig. 3(c)]. Figure 3(a) displays the quantum oscillations in the magnetoresistance ΔR_{xx} of a 25-nm-thick bismuth film, measured at various tilt angles ranging from 0° to 70.5°. Indeed, the quantum oscillation frequencies f_e and f_h, corresponding to electrons and holes, respectively, follow linear relations with $1/\cos\theta$, i.e., $f_{e,h}(\theta) = f_{e,h}(0°)/\cos\theta$ [Fig. 3(b)]. To quantify the degree of two dimensionality in bismuth surface transport, we model the Fermi surface using a three-dimensional ellipsoidal geometry and define the mass anisotropy as the ratio between the out-of-plane and in-plane effective mass $m_z/m_{\|}$. We find that lower bounds of the mass anisotropy

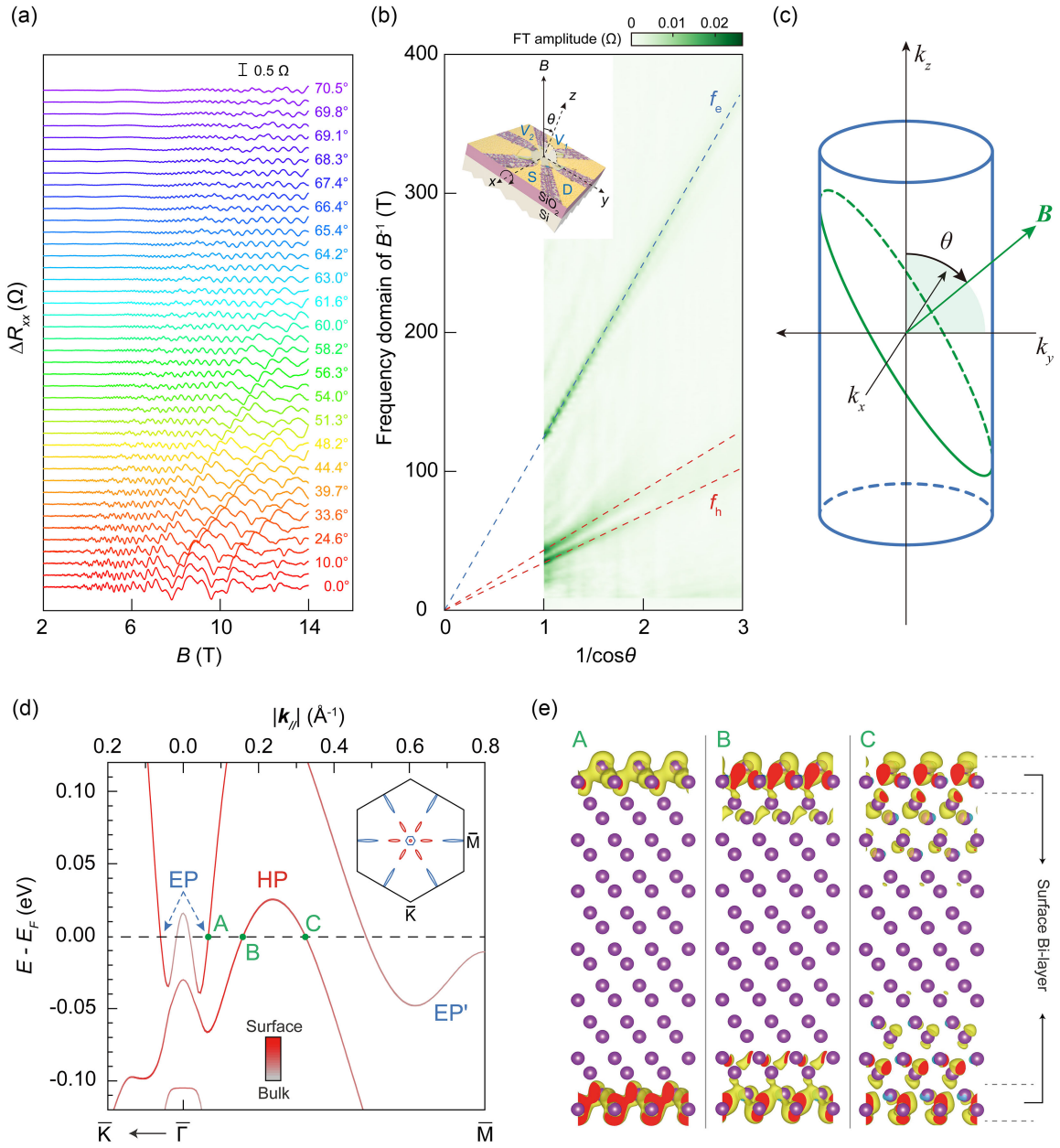


FIG. 3. Angle dependence of the quantum oscillations in bismuth 2DES. (a) Quantum oscillations in a Bi/hBN heterostructure with a nominal bismuth thickness of 25 nm, measured at various tilt angles θ (values indicated on the right). Data were obtained at $T = 1.5$ K and $V_g = 0$ V. (b) Fourier transform (FT) amplitude of $\Delta R_{xx}(B^{-1})$ plotted as a function of both the inverse total magnetic field frequency and $1/\cos\theta$. The blue (f_e) and red (f_h) dashed lines trace the FT peaks corresponding to Fermi surface area $A(\theta)$ of electrons and holes, respectively. The splitting of the f_h line into two branches indicates broken rotational symmetry among the six hole pockets (see Sec. V). The observed linear relation $A(\theta) = A(0)/\cos\theta$ confirms the cylindrical shape of the Fermi surfaces for both electron and hole carriers. (c) Schematic of the cylindrical Fermi surface in a titled magnetic field. The green circle marks the extremal cross section perpendicular to the field direction. We take k_x and k_y along the $\overline{\Gamma K}$ and $\overline{\Gamma M}$ directions respectively, and k_z perpendicular to the film surface. The tilting of the magnetic field is controlled within the k_z-k_y plane. (d) DFT electronic band structure of a ten-layer bismuth slab along the $\bar{K} - \bar{\Gamma} - \bar{M}$ direction. The bands are color coded to reflect the amplitude of their surface projection. The top-right inset shows the calculated Fermi surface [see also Fig. S8(a)], where the blue (red) lines represent electron (hole) states. (e) Side view of the calculated charge density distribution of states A, B, and C indicated in panel (d).

for EP and HP carriers exceed 3900 and 1700, respectively (details of the analysis are provided in Appendix A). These results establish that the bismuth thin films grown on hBN host a high-mobility 2DES on their surfaces.

To further examine where the bismuth electron states are located in the real space, we perform *ab initio* density functional theory (DFT) calculations of the electronic structure of a ten-layer bismuth slab (thickness of around 4 nm). Details of the DFT calculations are given in Appendix C 3. We note that the bands crossing Fermi level are indeed primarily surface bands (EP and HP) [Fig. 3(d)]. The charge density distribution of representative states on EP and HP at the Fermi level is shown in Fig. 3(e). The state labeled by A, which is responsible for the quantum oscillations from the EP, resides in the first atomic layer on the bismuth top and bottom surfaces. States B and C, responsible for the quantum oscillation from the HP, are similarly located in the 2–3 surface layers. These results corroborate the 2D nature of the EP and HP that we observe in our experiments. Additionally, states on the other electron pockets (EP′) near $\bar{\mathrm{M}}$ points and the tiny hole pocket at $\bar{\Gamma}$ extend deeply into the bulk (see Sec. 10 in Supplemental Material [68]), and we do not observe quantum oscillations from them.

IV. SOC AND LL DEGENERACY IN BISMUTH 2DES

One of the defining characteristics of the bismuth 2DES is its strong SOC, which may enable novel topological quantum states, such as the high-temperature quantum spin Hall effect [40,44]. Angle-resolved photoemission spectroscopy measurements on bulk and thin-film bismuth have revealed that their surface states arise from Rashba-type SOC, which fully lifts the spin degeneracy [59,60]. As a result, each Rashba surface state carries only one spin-momentum-locked electron.

Our analysis of gate-dependent quantum oscillations provides direct transport evidence for the complete spin lifting of the hole carriers in bismuth 2DES. We determine the degeneracy of the hole pockets by comparing the carrier density change inferred from the quantum oscillations to the gate-induced doping. Specifically, under back gate modulation, the carriers doped into the six HPs can be obtained as $\Delta n_{\mathrm{h}} = 6(\Delta A_{\mathrm{h}}/4\pi^2)$, where $\Delta A_{\mathrm{e,h}}$ is the gate-induced change in the Fermi surface area extracted from the quantum oscillations. On the other hand, the total gate doping can be independently obtained via $\Delta n_{\mathrm{g}} = C_{\mathrm{g}} V_{\mathrm{g}}$, where C_{g} is the geometric capacitance per unit area of the gate dielectric. For the device shown in Fig. S5, the gate dielectric of 12-nm-thick hBN ($\varepsilon_{\mathrm{r}} \approx 4$) and 285-nm-thick SiO_2 ($\varepsilon_{\mathrm{r}} \approx 3.9$) yields a C_{g} of $7.26 \times 10^{10}\ e\,\mathrm{cm}^{-2}\,\mathrm{V}^{-1}$ [25,31]. We find $\Delta n_{\mathrm{g}} \approx -(1.84 \pm 0.05) \times \Delta n_{\mathrm{h}}$. Assuming the HPs have a spin degeneracy γ, the prefactor 1.84 constrains γ to be less than 2 and uniquely determines $\gamma = 1$. This result confirms that the HPs are nondegenerate and fully spin split due to strong Rashba SOC (see Sec. 11 in Supplemental Material [68]).

The observed single degeneracy of hole LLs also implies an asymmetry between the top and bottom surfaces—the quantum oscillations from the top surface are notably missing, an absence we attribute to the insufficient mobility of the top surface carriers. This surface asymmetry is further corroborated by results from hBN/Bi/hBN heterostructures (see Sec. 8, Supplemental Material [68]), where the hBN capping layer improves the quality of the bismuth film's top surface. In these samples, we observe an additional set of quantum oscillations from the top surface. The oscillation frequency is independent of back gate voltage (Fig. S13), consistent with the expectation that the gate field is fully screened by the bottom-surface carriers.

V. QUANTUM TRANSPORT IN BISMUTH 2DES

The high quality of the bismuth film on hBN offers a precious opportunity to investigate the dual-carrier transport in bismuth 2DES with both electrons and holes under extreme quantum conditions. By applying a large magnetic field as high as 40 T, we simultaneously drive both electrons and holes into the lowest few LLs, thereby reaching the extreme quantum limit. Previously, this regime had only been accessed in STM studies [12,64], and our work represents the first transport measurement of bismuth 2DES in this limit. Figure 4(a) displays the oscillatory magnetoresistance ΔR_{xx} recorded as a function of both back gate voltage V_{g} and perpendicular magnetic field B. The LLs, manifesting as lines that trace the ΔR_{xx} maxima, are clearly identified for both electrons and holes. These LLs become more pronounced in the magnetoresistance's second derivative, $\partial^2 R_{xx}/\partial V_{\mathrm{g}}^2$, plotted in Fig. 4(b). Using Středa's formula [85], we identify the filling factors of the lowest LLs, reaching as low as $\nu_{\mathrm{e}} = 3$ for electrons and $\nu_{\mathrm{h}} = 4$ for holes (see Appendix B).

A prominent feature of quantum transport in the bismuth 2DES is the splitting of the hole LLs, which are initially sixfold degenerate. This degeneracy originates from the six equivalent oblong HPs aligned along the $\overline{\Gamma\mathrm{M}}$ directions [inset of Fig. 3(d)]; its lifting therefore signifies a breaking of the C_6 rotational symmetry. As shown in Figs. 4(b), S7(a), and 3(b), splitting of the hole LLs is already visible at fields as low as around 8 T. At higher magnetic fields above around 15 T, each hole LL is observed to split into three [Fig. 4(b)], so the hole LLs now become twofold degenerate, leaving a residual twofold degeneracy and indicating that the C_6 symmetry of the HPs is reduced to C_2. This LL splitting is consistent with previous STM studies on cleaved bulk Bi(111) surfaces, where the rotational symmetry breaking was attributed to strain and/or electronic nematicity [12]. The strong resemblance between the STM and transport observations suggests that similar symmetry-breaking mechanisms may be at play in the bismuth 2DES of thin bismuth films. Indeed, when a field-independent energy splitting of 4.3 meV among the three HPs is incorporated, our simulation of the 2DES density of states (DOS) at the

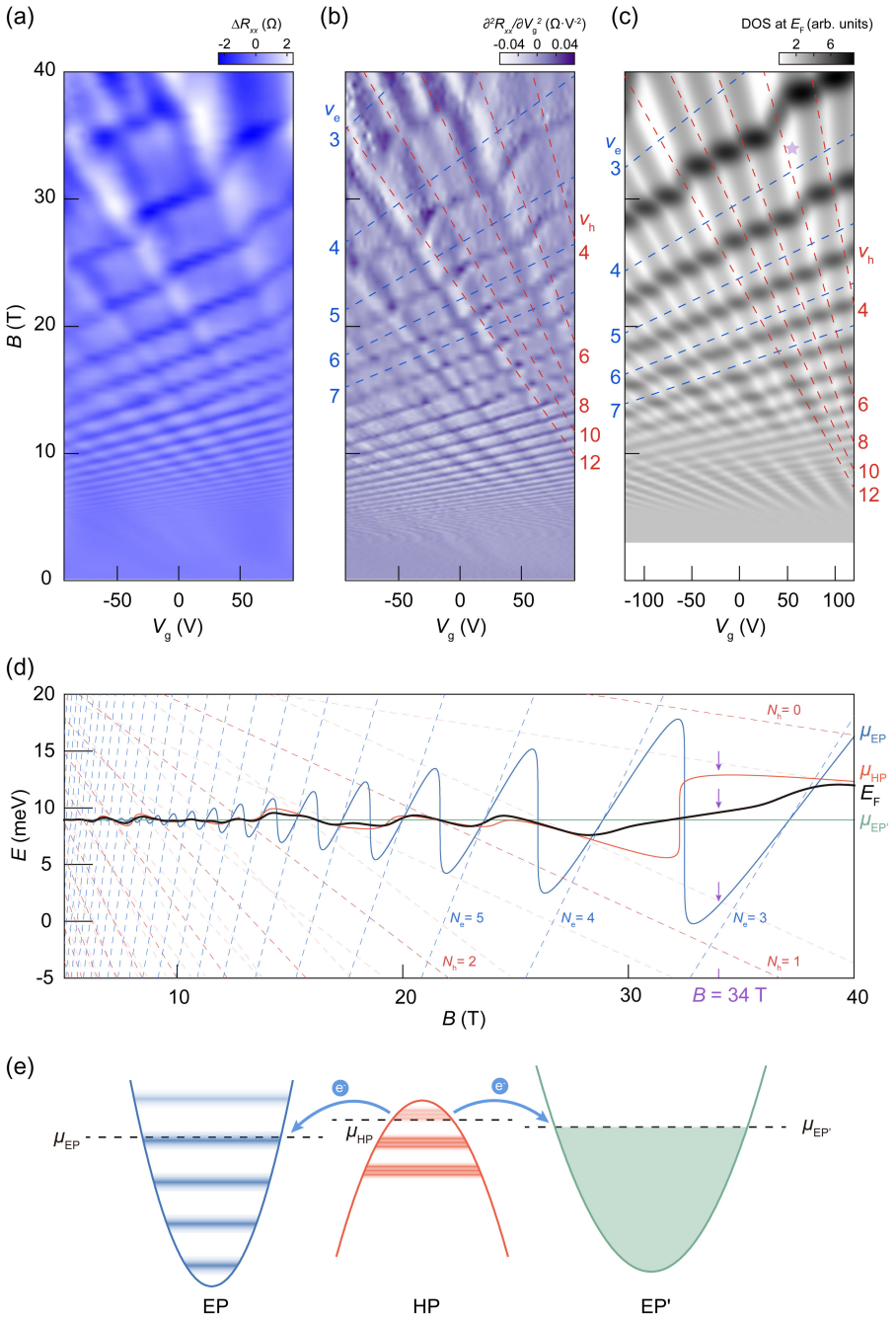


FIG. 4. Electronic transport in bismuth 2DES in the extreme quantum limit. (a) Oscillatory part of the magnetoresistance, ΔR_{xx}, of a bismuth 2DES plotted as a function of both B and V_g. Data were obtained at $T = 0.3$ K. (b) Second derivative of the magnetoresistance, $\partial^2 R_{xx}/\partial V_g^2$, plotted as a function of both B and V_g. Plots in (a) and (b) are derived from the same magnetoresistance data set obtained in a Bi/hBN heterostructure with nominally 10-nm-thick bismuth. The blue and red dashed lines mark the filling factors for electrons (ν_e) and holes (ν_h), respectively. (c) Simulated DOS at Fermi level (normalized to the zero-field DOS), plotted as a function of B and V_g. The simulation directly correlates with the R_{xx} variations shown in panels (a) and (b). (d) Illustration of the carrier migration mechanism. Blue and red dashed lines represent the LL dispersion of carriers at the EP and HPs, respectively, under a fixed gate of $V_g = 55$ V; a field-independent hole valley splitting of 4.3 meV is included in the dispersion. Blue (μ_{EP}) and red (μ_{HP}) solid lines show the chemical potentials of carriers at the EP and HPs, respectively, assuming the two carrier types are considered separately. The differing μ_{EP} and μ_{HP} drive the carriers to migrate from high-energy pockets to low-energy ones, reaching an equilibrium Fermi level E_F that is represented by the black solid line. A constant DOS is assumed for the carriers at the EP′ pockets, resulting in a nearly constant chemical potential, $\mu_{EP'}$ (green solid line). The arrows indicate a representative field value, $B = 34$ T, marked by the purple star in panel (c). (e) Schematic of the carrier migration process under a representative situation, $B = 34$ T and $V_g = 55$ V, marked by the purple star in panel (c).

Fermi level accurately reproduces the observed LL splitting across the entire magnetic-field range [Fig. 4(c); details in Appendix C 4]. This result points to a strain-induced origin —consistent with the field independence of the splitting— although possible contributions from electronic nematicity cannot be completely excluded.

Our simulation also captures another key feature of the dual-carrier transport in the bismuth 2DES—the zigzag patterns formed by intersecting electron and hole LLs [Figs. 4(b) and 4(c)]. These zigzag patterns are in stark contrast to the straight lines expected in single-carrier quantum transport, as indicated by the dashed lines in Figs. 4(b) and 4(c). This anomalous behavior can be understood by analyzing the chemical potentials of both electrons and holes in the quantum limit. As illustrated in Fig. 4(d), when each carrier type is considered independently, its chemical potential intermittently follows the LL dispersion to maintain a constant carrier density as the magnetic field increases, resulting in a characteristic sawtoothlike variation [2,86,87]. However, given that all carriers reside within the same 2DES, the differing chemical potentials (blue and red curves for EP and HP carriers, respectively) drive carriers to migrate from high-energy pockets to lower-energy pockets until a common Fermi level is reached (black curve). A representative migration process is schematically illustrated in Fig. 4(e). This carrier redistribution alters the apparent carrier density in each pocket and produces the observed zigzag pattern. Finally, we note that such carrier migration is a generic feature of multicarrier systems. A hint of this process is visible in the tunneling spectroscopy of cleaved bulk Bi(111) surfaces under magnetic fields [12], and similar phenomena have been reported in various other multicarrier systems [16,88–92].

VI. CONCLUSIONS

To conclude, we have established that the bismuth surface state forms a high-mobility, strongly spin-orbit coupled 2DES at the sharp crystalline Bi/hBN interface achieved via vdW epitaxy. This 2DES hosts both electron and hole carriers, which can be simultaneously driven into the extreme quantum limit under high magnetic fields. We observe that the C_6 symmetry of the hole carriers is reduced to C_2 and that carrier migration between Fermi pockets leads to an anomalous LL dispersion with zigzag patterns. Given its high mobility and significant SOC, the bismuth 2DES presents a promising avenue for exploring novel topological quantum states that exhibit a large energy scale, potentially robust at high temperatures [40].

ACKNOWLEDGMENTS

We thank Zengwei Zhu, Yijun Yu, Zihan Xu, Zhanting Li, Changqing Song, Ziyue Xu, Dawei Shen, Yichen Yang, Zhongkai Liu, Han Gao, and Hanbo Xiao for helpful discussions. Part of the sample fabrication was conducted at the Nano-fabrication Laboratory at Fudan University. We thank the Hybrid Magnet of the Steady High Magnetic Field Facility, CAS [93] for the assistance on the experiment. D. Y., H. W., Z. H., P. Z., Y. S., S. G., N. T., M. L., Z. G., H. L., W. R., and Y. Z. acknowledge support from the National Key R&D Program of China (Grant No. 2022YFA1403301), the National Science Foundation of China (Grant No. 1235000130), and the Shanghai Municipal Science and Technology Commission (Grants No. 23JC1400600 and No. 2019SHZDZX01). D. Y. also acknowledges support from the National Natural Science Foundation of China (Grant No. 12004075) and the China Postdoctoral Science Foundation (Grants No. BX20190084 and No. 2019M661330). W. R. also acknowledges support from National Science Foundation of China (Grants No. 12274087 and No. 12350401). X. J. acknowledges support from the National Key Research and Development Program of China (Grant No. 2024YFA1408500). G. H. and C. Z. acknowledge support from the National Science Foundation of China (Grant No. 62171136). Y. J. and J. W. acknowledge support from the National Science Foundation of China (Grants No. 12350404 and No. 12174066), and the Shanghai Municipal Science and Technology Commission (Grants No. 23JC1400600, No. 24LZ1400100, and No. 2019SHZDZX01). C. X. and G. K. acknowledge support from the Systematic Fundamental Research Program Leveraging Major Scientific and Technological Infrastructure, Chinese Academy of Sciences under Contract No. JZHKYPT-2021-08. K. W. and T. T. acknowledge support from the JSPS KAKENHI (Grants No. 21H05233 and No. 23H02052) and the World Premier International Research Center Initiative (WPI), MEXT, Japan. Z. C. and X. L. acknowledge support from the National Key Research and Development Program of China (Grant No. 2021YFA1401900). This work has been supported by the New Cornerstone Science Foundation.

Y. Z., W. R., X. J., C. Z., and J. W. supervised the project. D. Y. and H. W. grew the bismuth thin films, performed AFM and Raman spectroscopy characterization, fabricated devices, and performed transport measurements. P. Z., Y. S., and S. G. helped with the growth of bismuth thin films. S. G., N. T., M. L., and Z. G. helped with the device fabrication and transport measurements. Z. H., N. T., H. L., and W. R. performed STM characterization. G. H. and C. Z. performed TEM characterization. Y. J. and J. W. carried out band structure calculations. C. X. and G. K. helped with the transport measurements in high magnetic fields at the High Magnetic Field Laboratory, HFIPS, Chinese Academy of Sciences. Z. C. and X. L. helped with the transport measurements at ultralow temperatures. K. W. and T. T. grew the bulk hBN crystals. D. Y., H. W., W. R., and Y. Z. analyzed the data and wrote the manuscript with input from all authors. All authors have given approval for the final version of the manuscript.

APPENDIX A: MAPPING THE FERMI SURFACE IN TILTED MAGNETIC FIELD

We establish the strictly two-dimensional nature of the surface transport in bismuth thin films by mapping out the Fermi surface shapes of the system. This goal is achieved by analyzing the tilt-angle dependence of the quantum oscillations measured in a titled magnetic field. The tilting of the magnetic field is controlled within the trigonal-bisectrix plane (the k_z-k_y plane) of the bismuth crystal as

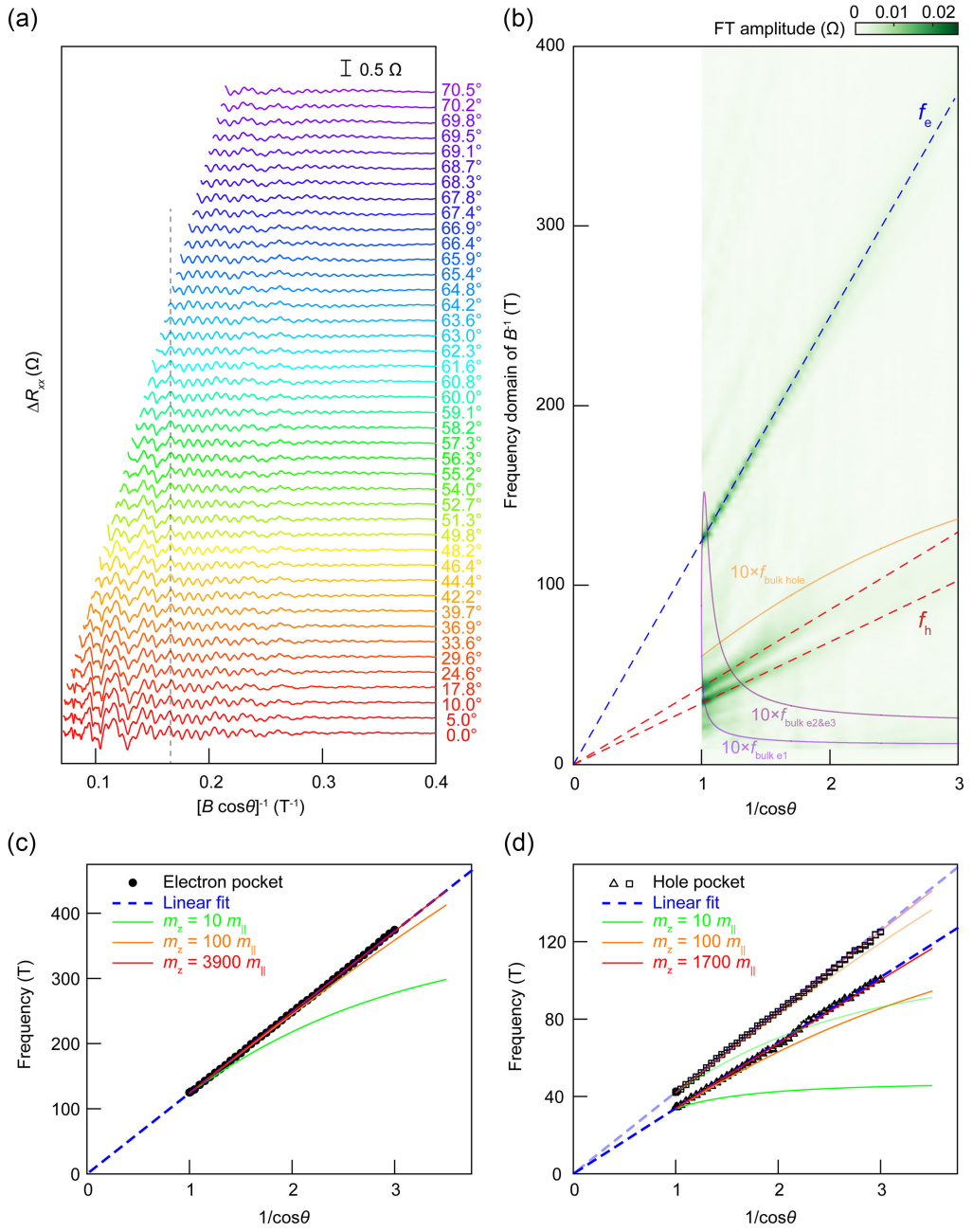


FIG. 5. Fermi surface mapping via magnetic-field tilt-angle dependence of quantum oscillations in the Bi/hBN heterostructure. (a) ΔR_{xx}, of the Bi(25 nm)/hBN heterostructure plotted as a function of $B_\perp^{-1} = [B\cos\theta]^{-1}$, at varying tilt angle θ [the same data set as that in Fig. 3(a)]. Values of θ are marked on the right side of each curve. The dashed line traces one representative peak at a certain $B_\perp^{-1}$. (b) Tilt-angle dependences of quantum oscillation frequencies in the Bi/hBN heterostructure [the same data set as that in Fig. 3(b)] compared with those in bulk bismuth states [1,97,98]. The yellow solid curve represents the bismuth bulk hole pocket (labeled as "bulk hole") centered at the T point with the long axis along the trigonal axis; the violet and purple solid curves represent the three bismuth bulk electron pockets centered at L points with the long axes tilted about 6° from the binary-bisectrix plane, with one (labeled as "bulk e1") lying in the k_z-k_y plane and the other two (labeled as "bulk e2 & e3") lying in the other two trigonal-bisectrix planes. The bulk-state data are magnified by 10 times for a better comparison with our data. (c),(d) Quantitative analyses of tilt-angle dependence of quantum oscillation frequencies of electron and hole carriers in the Bi/hBN heterostructure based on various models described in Appendix A.

indicated in Figs. 3(b) and 3(c). The tilt angle θ is defined as the angle between the magnetic field and the trigonal axis of the bismuth crystal; the latter is perpendicular to the film surface.

Hints of the 2D character of the electron system are already apparent from the quantum oscillations in ΔR_{xx}, plotted as a function of $B_\perp^{-1}$, where $B_\perp$ is the perpendicular field component $B_\perp = B\cos\theta$ [Fig. 5(a)]. All oscillatory features precisely align, exemplified by the dashed line in Fig. 5(a). This observation indicates that the surface transport through the bismuth electron system depends only on the perpendicular magnetic field component $B_\perp$, one of the key features of a 2DES [94–96].

The two dimensionality of bismuth electron systems is further evidenced by the linear relation between the oscillation frequencies and $1/\cos\theta$. Figure 5(b) replots the FT of the quantum oscillations from Fig. 3(b). It is clear that the 3D bulk states (solid lines) [1,97,98] do not contribute to the oscillations we observe. Instead, the linear behavior of the oscillation frequencies implies a cylindrical Fermi surface, i.e., 2D transport, for both electrons and holes (see Sec. III, main text). The high degree of linearity is reflected in the linear fits of f_e and f_h as functions of $1/\cos\theta$ shown in Figs. 5(c) and 5(d)—the adjusted coefficients of determination (R^2) for the linear fits of f_e and f_h reach 0.99999 and 0.99996, respectively.

To further quantify the strict 2D nature of the bismuth 2DES, we assume an out-of-plane effective mass m_z, in addition to the in-plane effective masses m_x and m_y, and establish a lower bound for m_z. Under this assumption, the extremal area A of the Fermi surface perpendicular to the magnetic field is given by

$$A = \pi \frac{abc}{\sqrt{b^2\sin^2\theta + c^2\cos^2\theta}}, \tag{A1}$$

when the magnetic field is along the direction $\hat{n} = (0, \sin\theta, \cos\theta)$, where $a = \sqrt{((2E_F m_x)/\hbar^2)}$, $b = \sqrt{((2E_F m_y)/\hbar^2)}$, $c = \sqrt{((2E_F m_z)/\hbar^2)}$, and E_F is the Fermi level counted from the band bottom (or top) of EP (or HPs). For the EP centered at the $\bar{\Gamma}$ point, $m_x^{EP} = m_y^{EP}$, which we denote with $m_{||}^{EP}$. The out-of-plane effective mass for the EP can be expressed as $m_z^{EP} = \beta_{EP} m_{||}^{EP}$, with β_{EP} quantifying the effective mass anisotropy. For each choice of β_{EP}, we treat the simulated angle dependence of f_e as a fit to the experimental data and calculate the R^2 [Fig. 5(c)]. It turns out that a minimum β_{EP} of around 3900 is required to achieve a R^2 comparable to that of the linear fit. This requirement sets a lower bound for the effective mass anisotropy of the EP. For the oblong HPs along the k_y direction, we take $m_{||}^{HP} = \sqrt{m_x^{HP} m_y^{HP}}$ (the values of m_x^{HP} and m_y^{HP} are taken from our DFT calculations) and denote $m_z^{HP} = \beta_{HP} m_{||}^{HP}$. A similar analysis yields a lower bound of $\beta_{HP} \sim 1700$ for HP [Fig. 5(d)]. The large anisotropy values are 2 orders of magnitude higher than those of bulk carriers in bismuth and graphite [99,100], and thus we establish that the surface states on bismuth thin films form a strictly 2D electron system.

APPENDIX B: DETERMINING THE LL FILLING FACTORS

We determine the LL filling factors from the slope of the lines tracing ΔR_{xx} maximum in the Landau fan diagram according to Středa's formula [85]:

$$\nu_e = \frac{h}{e}\frac{\Delta n_e}{\Delta B}, \qquad \nu_h = \frac{h}{e}\frac{\Delta n_h}{\Delta B}, \tag{B1}$$

where h is the Plank constant, and $\Delta n_e = (\Delta A_e/4\pi^2)$ and $\Delta n_h = 6(\Delta A_h/4\pi^2)$ are changes in electron and hole carrier densities inferred from the quantum oscillations, respectively. Here, an integer filling factor corresponds to ΔR_{xx} maxima (i.e., $\Delta\sigma_{xx}$ minima) [Fig. 6(a)].

To extract the ΔR_{xx} maxima for electrons and holes separately, we apply Fourier bandpass filters [101] to the quantum oscillation data shown in Fig. 6(b). Line fits of the LLs at low fields are presented as blue and red lines in Fig. 6(c), yielding both the electron and hole filling factors, respectively. In particular, the hole filling factors are obtained as multiples of 6, the number of hole valleys on the bottom surface of the bismuth film [Fig. S8(a)].

Here, the low-field (less than 14 T) quantum oscillation data are used for the analysis to avoid uncertainties caused by the zigzag pattern in the Landau fan diagram at high fields. We then obtain the high-field filling factors [dashed lines in Fig. 4(b)] by extrapolating the fitting results at low magnetic fields.

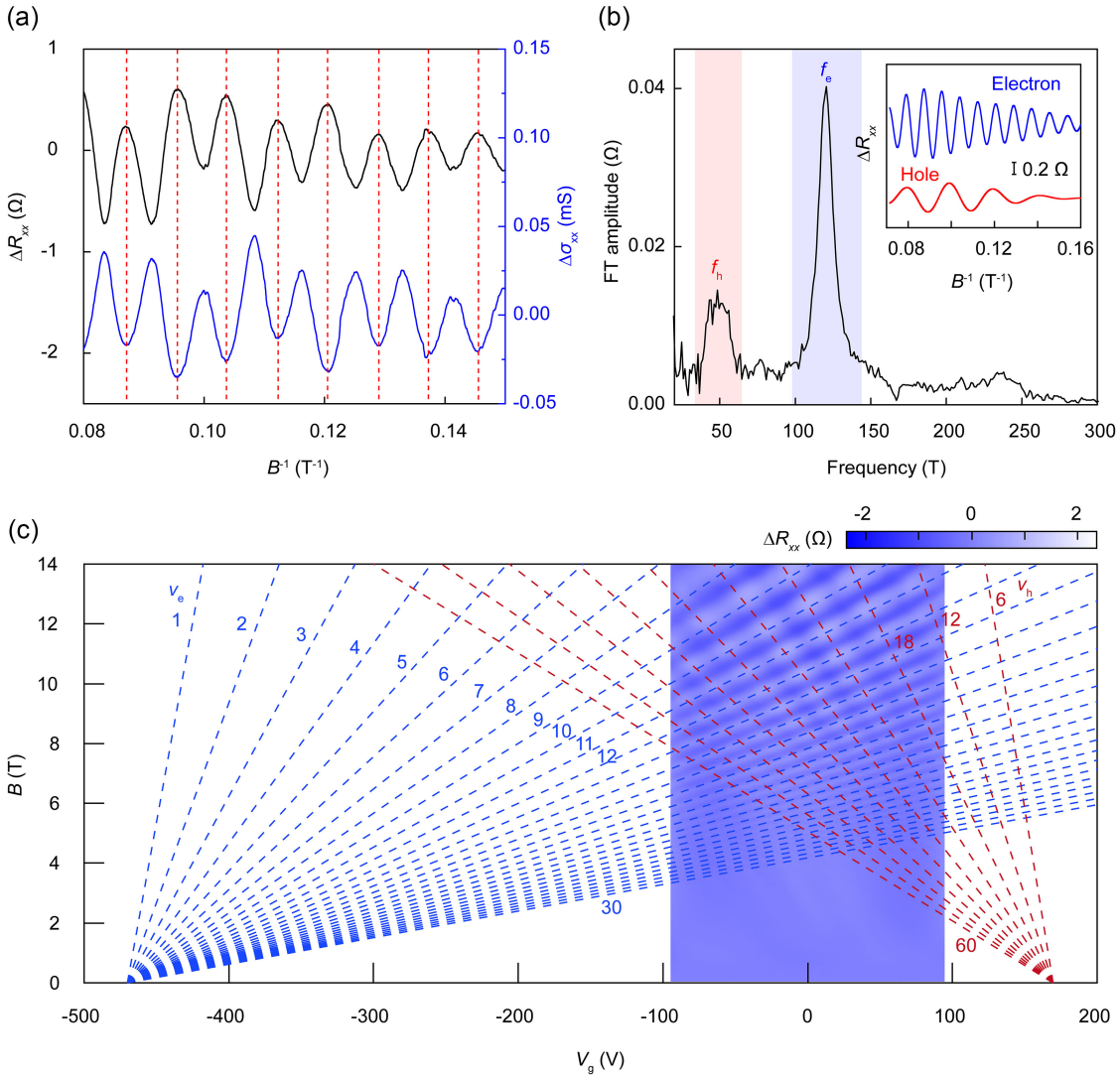


FIG. 6. Determining the LL filling factors. (a) Quantum oscillations in ΔR_{xx} (black) and $\Delta\sigma_{xx}$ (blue). Data were obtained from the same sample shown in Fig. 4 at $T = 1.5$ K and $V_g = 0$. The red dashed lines mark the local maxima (minima) of ΔR_{xx} ($\Delta\sigma_{xx}$). (b) Fourier transform of the ΔR_{xx} quantum oscillation data in panel (a). The two peaks are associated with the electron and hole pockets. The inset shows the quantum oscillations from electrons and holes separately, obtained from the data in panel (a) by applying two separate Fourier bandpass filters. The two bandpass filters are marked in the main panel. (c) Landau fan diagram of the low-field quantum oscillations. Blue and red lines represent line fits of the electron and hole LLs, respectively.

APPENDIX C: METHODS

1. Sample protection during characterization and device fabrication

All samples used in our experiments were rigorously protected from exposure to ambient air throughout the entire fabrication and measurement process. Specifically, the bismuth films were grown under UHV conditions. All subsequent fabrication steps were conducted in an argon-filled glovebox with oxygen and moisture levels maintained below 0.1 ppm. Sample characterizations—including Raman spectroscopy and AFM—were performed inside the glovebox, while low-temperature transport measurements were carried out in a sealed sample space filled with high-purity helium gas. During transfers between the UHV chamber, glovebox, and transport setup, the samples were carefully sealed to avoid any air exposure.

2. STEM characterization of the Bi/hBN heterostructure

To perform the aberration-corrected STEM measurements on the cross section of the Bi/hBN sample, we prepared the specimens with a focused ion beam (FIB) system. Atomic resolution STEM images were taken with a field emission scanning transmission electron microscope (Themis Z, Thermo Fisher Scientific) operating at 300 kV. The geometric aberrations of the probe-forming lens within

the aperture were tuned to zero with a probe corrector (SCORR, CEOS GmbH). The probe's semiconvergence angle was set at 21.4 mrad. The semicollection angle for the annular dark field detector ranged from 49 mrad to 200 mrad, while the bright field detector's semicollection angle was 28 mrad. A fast-scanning rate (0.5 μs dwell time) was used to acquire the STEM images and minimize the sample drift effect. Finally, 20 frames were integrated using a rigid-body drift correction algorithm to produce the drift-corrected STEM images.

3. DFT calculation of the band structure of the bismuth thin slab

The geometry optimization and electronic structure calculations were carried out by the Vienna *ab initio* simulation package [102] with the projector augmented wave method [103]. The exchange-correlation energy is described by the generalized gradient approximation (GGA) in the Perdew-Burke-Ernzerhof parametrization [104]. The energy cutoff for the plane-wave expansion was set to 500 eV, and a vacuum space of 20 Å was used to exclude the interactions caused by the periodic boundary condition. The energy convergence criteria were set to 10^{-7} eV. The Γ-centered Monkhorst-Pack k-point meshes $19 \times 19 \times 1$ were adopted for the bismuth ten-layer unit cell. The van der Waals interaction functional using the method of zero damping DFT-D3 was employed [105]. The lattice constant 4.53 Å was taken from experiment; the same results were also reported in previous work [64].

4. Simulation of quantum oscillations in the bismuth 2DES

The quantum oscillation of ΔR_{xx} was simulated by computing the Fermi-level DOS of the bismuth 2DES under strong magnetic fields [Fig. 4(c)]. Here, the relevant electronic states that exhibit quantum oscillations included one EP at the $\bar{\Gamma}$ point and six HPs along the $\overline{\Gamma M}$ directions, all of them from the bottom surface, as determined by our experiment and DFT calculations. To compute the Fermi-level DOS, we first solved the equation

$$\int_0^{\mu} \mathrm{DOS}(E,B)\mathrm{d}E = \Delta n_{\mathrm{g}} \tag{C1}$$

numerically to obtain the Fermi energy $\mu(B, \Delta n_{\mathrm{g}})$ as a function of magnetic field B and gate doping $\Delta n_{\mathrm{g}} = C_{\mathrm{g}} V_{\mathrm{g}}$, where $\mathrm{DOS}(E,B)$ is the DOS at energy E under field B. The Fermi-level DOS was then obtained from $\mathrm{DOS}(E=\mu,B)$. To find the function $\mathrm{DOS}(E,B)$, we formulated the energy spectrum of the LLs formed in the EP and HPs by

$$\begin{cases} E_{\mathrm{LL,EP}}(N_{\mathrm{EP}},B) = \varepsilon_{\mathrm{e0}} + \left(N_{\mathrm{EP}} + \frac{1}{2}\right)\hbar\frac{eB}{m^*_{\mathrm{EP}}} \\ E_{\mathrm{LL,HP}}(N_{\mathrm{HP}},B) = \varepsilon_{\mathrm{h0}} - \left(N_{\mathrm{HP}} + \frac{1}{2}\right)\hbar\frac{eB}{m^*_{\mathrm{HP}}} + \Delta_{\mathrm{split}} \end{cases}, \tag{C2}$$

where N_{EP} and N_{HP} are the LL indices, $\hbar$ is the reduced Planck constant, and e is the elementary charge. The effectives masses $m^*_{\mathrm{EP}} = 0.13m_0$ and $m^*_{\mathrm{HP}} = 0.19m_0$ used in the simulation were determined from experiment and DFT calculations (see Sec. 6 in Supplemental Material [68]). The EP-band bottom energy $\varepsilon_{\mathrm{e0}} = -108.5$ meV and the HP-band top energy $\varepsilon_{\mathrm{h0}} = 28.6$ meV were taken such that the predicted quantum oscillation frequencies agreed with the experimentally measured values at $V_{\mathrm{g}} = 0$. An additional level splitting $\Delta_{\mathrm{split}} = 0, \pm\Delta$ was applied to the HPs, whose value was estimated as $\Delta = (\hbar e/m^*_{\mathrm{HP}})\Delta f_{\mathrm{HP}} = 4.3$ meV, where $\Delta f_{\mathrm{HP}} = 7.1$ T is the quantum oscillation frequency splitting at $\theta = 0°$ read from Fig. 3(b). For convenience, we assumed a Gaussian broadening for each LL,

$$G(E,E_0,\Gamma) = \frac{1}{\sqrt{2\pi}\Gamma} e^{-\frac{(E-E_0)^2}{2\Gamma^2}}, \tag{C3}$$

and the DOS can be written as

$$\begin{aligned} &\mathrm{DOS}(E,B) \\ &= \sum_{N_{\mathrm{EP}}\geq 0} \frac{eB}{h} G(E, E_{\mathrm{LL,EP}}(N_{\mathrm{EP}},B), \Gamma_{\mathrm{EP}}) \\ &\quad + \sum_{N_{\mathrm{HP}}\geq 0, \Delta_{\mathrm{split}}=0,\pm\Delta} \frac{2eB}{h} G(E, E_{\mathrm{LL,HP}}(N_{\mathrm{HP}},B), \Gamma_{\mathrm{HP}}), \end{aligned} \tag{C4}$$

where the broadenings are estimated as $\Gamma_{\mathrm{EP}} = (\hbar/\tau_{\mathrm{e}}) = 5.2$ meV and $\Gamma_{\mathrm{HP}} = (\hbar/\tau_{\mathrm{h}}) = 2.1$ meV (see Sec. 6 in Supplemental Material [68]). For the EP, the areal degeneracy was (eB/h), while for the HPs, the areal degeneracy was $(2eB/h)$ because each split hole branch contained two LLs from the original six degenerated HP valleys [Fig. S8(a)].

An alternative way to understand the exotic quantum oscillation behavior [Fig. 4(c)] is by starting from decoupled 2D electron and hole gases, which are filled with charge carriers separately upon gate tuning. This approach would otherwise lead to straight lines in the LL fan diagram, as well as oscillating unbalanced chemical potentials [μ_{EP} and μ_{HP} in Figs. 4(d) and 4(e)]. Carrier migration among the pockets thus occurs, finally reaching an equilibrium chemical potential [E_F in Fig. 4(d)]; the zigzag patterns emerge as a result [Figs. 4(a)–4(c)].

[1] V. S. Édel'man, *Electrons in bismuth*, Adv. Phys. **25**, 555 (1976).
[2] D. Shoenberg, *Magnetic Oscillations in Metals* (Cambridge University Press, Cambridge, England, 1984).
[3] N. W. Ashcroft and N. D. Mermin, *Solid State Physics* (Holt, Rinehart and Winston, New York, 1976).

[4] A. Brugmans, *Antonii Brugmans Magnetismus, seu, De affinitatibus magneticis observationes academicæ* (Apud Luzac & Van Damme, Leiden, 1778).

[5] A. v. Ettingshausen and W. Nernst, *Ueber das Auftreten electromotorischer Kräfte in Metallplatten, welche von einem Wärmestrome durchflossen werden und sich im magnetischen Felde befinden*, Ann. Phys. (Berlin) **265**, 343 (1886).

[6] L. Shubnikov and W. J. de Haas, *Magnetische Widerstandsvergrösserung in Einkristallen von Wismut bei tiefen Temperaturen*, Proc. R. Neth. Acad. Arts Sci. **33**, 130 (1930), https://dwc.knaw.nl/DL/publications/PU00014617.pdf.

[7] W. J. de Haas and P. M. van Alphen, *The dependence of the susceptibility of diamagnetic metals upon the field*, Proc. R. Neth. Acad. Arts Sci. **33**, 1106 (1930), https://dwc.knaw.nl/DL/publications/PU00014621.pdf.

[8] X.-L. Qi and S.-C. Zhang, *Topological insulators and superconductors*, Rev. Mod. Phys. **83**, 1057 (2011).

[9] B. Jäck, Y. Xie, J. Li, S. Jeon, B. A. Bernevig, and A. Yazdani, *Observation of a Majorana zero mode in a topologically protected edge channel*, Science **364**, 1255 (2019).

[10] S. Ito *et al.*, *Proving nontrivial topology of pure bismuth by quantum confinement*, Phys. Rev. Lett. **117**, 236402 (2016).

[11] Y. Fukushima *et al.*, *Spin-polarized saddle points in the topological surface states of elemental bismuth revealed by pump-probe spin- and angle-resolved photoemission spectroscopy*, Phys. Rev. B **110**, L041401 (2024).

[12] B. E. Feldman, M. T. Randeria, A. Gyenis, F. Wu, H. Ji, R. J. Cava, A. H. MacDonald, and A. Yazdani, *Observation of a nematic quantum Hall liquid on the surface of bismuth*, Science **354**, 316 (2016).

[13] K. Behnia, L. Balicas, and Y. Kopelevich, *Signatures of electron fractionalization in ultraquantum bismuth*, Science **317**, 1729 (2007).

[14] L. Li, J. G. Checkelsky, Y. S. Hor, C. Uher, A. F. Hebard, R. J. Cava, and N. P. Ong, *Phase transitions of Dirac electrons in bismuth*, Science **321**, 547 (2008).

[15] O. Prakash, A. Kumar, A. Thamizhavel, and S. Ramakrishnan, *Evidence for bulk superconductivity in pure bismuth single crystals at ambient pressure*, Science **355**, 52 (2017).

[16] Z. Zhu, J. Wang, H. Zuo, B. Fauqué, R. D. McDonald, Y. Fuseya, and K. Behnia, *Emptying Dirac valleys in bismuth using high magnetic fields*, Nat. Commun. **8**, 15297 (2017).

[17] F. Schindler *et al.*, *Higher-order topology in bismuth*, Nat. Phys. **14**, 918 (2018).

[18] J. Gou, H. Bai, X. Zhang, Y. L. Huang, S. Duan, A. Ariando, S. A. Yang, L. Chen, Y. Lu, and A. T. S. Wee, *Two-dimensional ferroelectricity in a single-element bismuth monolayer*, Nature (London) **617**, 67 (2023).

[19] A. K. Geim, *Nobel lecture: Random walk to graphene*, Rev. Mod. Phys. **83**, 851 (2011).

[20] K. S. Novoselov, *Nobel lecture: Graphene: Materials in the flatland*, Rev. Mod. Phys. **83**, 837 (2011).

[21] T. Ando, A. B. Fowler, and F. Stern, *Electronic properties of two-dimensional systems*, Rev. Mod. Phys. **54**, 437 (1982).

[22] K. v. Klitzing, G. Dorda, and M. Pepper, *New method for high-accuracy determination of the fine-structure constant based on quantized Hall resistance*, Phys. Rev. Lett. **45**, 494 (1980).

[23] D. C. Tsui, H. L. Stormer, and A. C. Gossard, *Two-dimensional magnetotransport in the extreme quantum limit*, Phys. Rev. Lett. **48**, 1559 (1982).

[24] K. S. Novoselov, A. K. Geim, S. V. Morozov, D. Jiang, Y. Zhang, S. V. Dubonos, I. V. Grigorieva, and A. A. Firsov, *Electric field effect in atomically thin carbon films*, Science **306**, 666 (2004).

[25] K. S. Novoselov, A. K. Geim, S. V. Morozov, D. Jiang, M. I. Katsnelson, I. V. Grigorieva, S. V. Dubonos, and A. A. Firsov, *Two-dimensional gas of massless Dirac fermions in graphene*, Nature (London) **438**, 197 (2005).

[26] Y. Zhang, Y.-W. Tan, H. L. Stormer, and P. Kim, *Experimental observation of the quantum Hall effect and Berry's phase in graphene*, Nature (London) **438**, 201 (2005).

[27] C. R. Dean *et al.*, *Boron nitride substrates for high-quality graphene electronics*, Nat. Nanotechnol. **5**, 722 (2010).

[28] K. F. Mak, C. Lee, J. Hone, J. Shan, and T. F. Heinz, *Atomically thin* MoS_2*: A new direct-gap semiconductor*, Phys. Rev. Lett. **105**, 136805 (2010).

[29] B. Radisavljevic, A. Radenovic, J. Brivio, V. Giacometti, and A. Kis, *Single-layer* MoS_2 *transistors*, Nat. Nanotechnol. **6**, 147 (2011).

[30] L. Li, Y. Yu, G. J. Ye, Q. Ge, X. Ou, H. Wu, D. Feng, X. H. Chen, and Y. Zhang, *Black phosphorus field-effect transistors*, Nat. Nanotechnol. **9**, 372 (2014).

[31] L. Li *et al.*, *Quantum Hall effect in black phosphorus two-dimensional electron system*, Nat. Nanotechnol. **11**, 593 (2016).

[32] C. Gong *et al.*, *Discovery of intrinsic ferromagnetism in two-dimensional van der Waals crystals*, Nature (London) **546**, 265 (2017).

[33] B. Huang *et al.*, *Layer-dependent ferromagnetism in a van der Waals crystal down to the monolayer limit*, Nature (London) **546**, 270 (2017).

[34] Y. Deng *et al.*, *Gate-tunable room-temperature ferromagnetism in two-dimensional* Fe_3GeTe_2, Nature (London) **563**, 94 (2018).

[35] Y. Deng, Y. Yu, M. Z. Shi, Z. Guo, Z. Xu, J. Wang, X. H. Chen, and Y. Zhang, *Quantum anomalous Hall effect in intrinsic magnetic topological insulator* $MnBi_2Te_4$, Science **367**, 895 (2020).

[36] Y. Yu, L. Ma, P. Cai, R. Zhong, C. Ye, J. Shen, G. D. Gu, X. H. Chen, and Y. Zhang, *High-temperature superconductivity in monolayer* $Bi_2Sr_2CaCu_2O_{8+\delta}$, Nature (London) **575**, 156 (2019).

[37] Y. Cao, V. Fatemi, S. Fang, K. Watanabe, T. Taniguchi, E. Kaxiras, and P. Jarillo-Herrero, *Unconventional superconductivity in magic-angle graphene superlattices*, Nature (London) **556**, 43 (2018).

[38] H. Park *et al.*, *Observation of fractionally quantized anomalous Hall effect*, Nature (London) **622**, 74 (2023).

[39] Ph. Hofmann, *The surfaces of bismuth: Structural, and electronic properties*, Prog. Surf. Sci. **81**, 191 (2006).

[40] S. Murakami, *Quantum spin Hall effect and enhanced magnetic response by spin-orbit coupling*, Phys. Rev. Lett. **97**, 236805 (2006).

[41] C. Sabater, D. Gosálbez-Martínez, J. Fernández-Rossier, J. G. Rodrigo, C. Untiedt, and J. J. Palacios, *Topologically protected quantum transport in locally exfoliated bismuth at room temperature*, Phys. Rev. Lett. **110**, 176802 (2013).

[42] K. Jiang, J. Ji, W. Gong, L. Ding, J. Li, P. Li, B. Li, and F. Geng, *Mechanical cleavage of non-van der Waals structures towards two-dimensional crystals*, Nat. Synth. **2**, 58 (2023).

[43] O. Yu, R. Allgayer, S. Godin, J. Lalande, P. Fossati, C. Hsu, T. Szkopek, and G. Gervais, *Method of mechanical exfoliation of bismuth with micro-trench structures*, J. Appl. Phys. **134**, 244302 (2023).

[44] F. Reis, G. Li, L. Dudy, M. Bauernfeind, S. Glass, W. Hanke, R. Thomale, J. Schäfer, and R. Claessen, *Bismuthene on a* SiC *substrate: A candidate for a high-temperature quantum spin Hall material*, Science **357**, 287 (2017).

[45] R. Stühler, A. Kowalewski, F. Reis, D. Jungblut, F. Dominguez, B. Scharf, G. Li, J. Schäfer, E. M. Hankiewicz, and R. Claessen, *Effective lifting of the topological protection of quantum spin Hall edge states by edge coupling*, Nat. Commun. **13**, 3480 (2022).

[46] A. Fang, C. Adamo, S. Jia, R. J. Cava, S.-C. Wu, C. Felser, and A. Kapitulnik, *Bursting at the seams: Rippled monolayer bismuth on* $NbSe_2$, Sci. Adv. **4**, eaaq0330 (2018).

[47] T. Hirahara, G. Bihlmayer, Y. Sakamoto, M. Yamada, H. Miyazaki, S. Kimura, S. Blügel, and S. Hasegawa, *Interfacing 2D and 3D topological insulators:* Bi(111) *bilayer on* Bi_2Te_3, Phys. Rev. Lett. **107**, 166801 (2011).

[48] M. Chen, J.-P. Peng, H.-M. Zhang, L.-L. Wang, K. He, X.-C. Ma, and Q.-K. Xue, *Molecular beam epitaxy of bilayer* Bi(111) *films on topological insulator* Bi_2Te_3*: A scanning tunneling microscopy study*, Appl. Phys. Lett. **101**, 081603 (2012).

[49] T. Nagao, J. T. Sadowski, M. Saito, S. Yaginuma, Y. Fujikawa, T. Kogure, T. Ohno, Y. Hasegawa, S. Hasegawa, and T. Sakurai, *Nanofilm allotrope and phase transformation of ultrathin* Bi *film on* $Si(111)-7\times7$, Phys. Rev. Lett. **93**, 105501 (2004).

[50] T. Nagao, S. Yaginuma, M. Saito, T. Kogure, J. T. Sadowski, T. Ohno, S. Hasegawa, and T. Sakurai, *Strong lateral growth and crystallization via two-dimensional allotropic transformation of semi-metal* Bi *film*, Surf. Sci. **590**, 247 (2005).

[51] H. Hirayama, *Nucleation and growth of ultrathin* Bi *films*, Adv. Phys. X **6**, 1845975 (2021).

[52] S. A. Scott, M. V. Kral, and S. A. Brown, *A crystallographic orientation transition and early stage growth characteristics of thin* Bi *films on HOPG*, Surf. Sci. **587**, 175 (2005).

[53] D. N. McCarthy, D. Robertson, P. J. Kowalczyk, and S. A. Brown, *The effects of annealing and growth temperature on the morphologies of* Bi *nanostructures on HOPG*, Surf. Sci. **604**, 1273 (2010).

[54] N. Hussain, T. Liang, Q. Zhang, T. Anwar, Y. Huang, J. Lang, K. Huang, and H. Wu, *Ultrathin* Bi *nanosheets with superior photoluminescence*, Small **13**, 1701349 (2017).

[55] L. Chen *et al.*, *Exceptional electronic transport and quantum oscillations in thin bismuth crystals grown inside van der Waals materials*, Nat. Mater. **23**, 741 (2024).

[56] J. Zhao *et al.*, *Realization of 2D metals at the ångström thickness limit*, Nature (London) **639**, 354 (2025).

[57] A. Koma, *Van der Waals epitaxy—a new epitaxial growth method for a highly lattice-mismatched system*, Thin Solid Films **216**, 72 (1992).

[58] C. R. Ast and H. Höchst, *Fermi surface of* Bi(111) *measured by photoemission spectroscopy*, Phys. Rev. Lett. **87**, 177602 (2001).

[59] Yu. M. Koroteev, G. Bihlmayer, J. E. Gayone, E. V. Chulkov, S. Blügel, P. M. Echenique, and Ph. Hofmann, *Strong spin-orbit splitting on* Bi *surfaces*, Phys. Rev. Lett. **93**, 046403 (2004).

[60] T. Hirahara, T. Nagao, I. Matsuda, G. Bihlmayer, E. V. Chulkov, Yu. M. Koroteev, P. M. Echenique, M. Saito, and S. Hasegawa, *Role of spin-orbit coupling and hybridization effects in the electronic structure of ultrathin* Bi *films*, Phys. Rev. Lett. **97**, 146803 (2006).

[61] Yu. M. Koroteev, G. Bihlmayer, E. V. Chulkov, and S. Blügel, *First-principles investigation of structural and electronic properties of ultrathin* Bi *films*, Phys. Rev. B **77**, 045428 (2008).

[62] S. Xiao, D. Wei, and X. Jin, Bi(111) *thin film with insulating interior but metallic surfaces*, Phys. Rev. Lett. **109**, 166805 (2012).

[63] K. Zhu, L. Wu, X. Gong, S. Xiao, and X. Jin, *Quantum transport in the surface states of epitaxial* Bi(111) *thin films*, Phys. Rev. B **94**, 121401 (2016).

[64] H. Du *et al.*, *Surface Landau levels and spin states in bismuth (111) ultrathin films*, Nat. Commun. **7**, 10814 (2016).

[65] A. G. F. Garcia, M. Neumann, F. Amet, J. R. Williams, K. Watanabe, T. Taniguchi, and D. Goldhaber-Gordon, *Effective cleaning of hexagonal boron nitride for graphene devices*, Nano Lett. **12**, 4449 (2012).

[66] Y. Yang, K. Xu, L. N. Holtzman, K. Yang, K. Watanabe, T. Taniguchi, J. Hone, K. Barmak, and M. R. Rosenberger, *Atomic defect quantification by lateral force microscopy*, ACS Nano **18**, 6887 (2024).

[67] S. Yaginuma, T. Nagao, J. T. Sadowski, A. Pucci, Y. Fujikawa, and T. Sakurai, *Surface pre-melting and surface flattening of* Bi *nanofilms on* $Si(111)-7\times7$, Surf. Sci. **547**, L877 (2003).

[68] See Supplemental Material at http://link.aps.org/supplemental/10.1103/hptx-pw9s, which includes Refs. [69–80], for additional data and analyses about AFM, STM, and STEM characterization of Bi/hBN and hBN/Bi/hBN heterostructures, magnetotransport and quantum oscillations observed in Bi/hBN and hBN/Bi/hBN heterostructures, and DFT electronic structure of the bismuth thin film (n.d.).

[69] Z. Jiang, V. Soghomonian, and J. J. Heremans, *Carrier properties of* Bi(111) *grown on mica and* Si(111), Phys. Rev. Mater. **6**, 095003 (2022).

[70] R. Ushioda, M. Shimura, K. Nakatsuji, and H. Hirayama, *Growth-rate dependence of the structural transition of bismuth islands on* Si(111) *substrates*, Phys. Rev. Mater. **6**, 043403 (2022).

[71] Y. Pan *et al.*, *Heteroepitaxy of semiconducting* 2H-$MoTe_2$ *thin films on arbitrary surfaces for large-scale heterogeneous integration*, Nat. Synth. **1**, 701 (2022).

[72] S. Y. F. Zhao *et al.*, *Time-reversal symmetry breaking superconductivity between twisted cuprate superconductors*, Science **382**, 1422 (2023).

[73] S. Guo *et al.*, *An ultra-high vacuum system for fabricating clean two-dimensional material devices*, Rev. Sci. Instrum. **94**, 013903 (2023).

[74] D. Abdelbarey, J. Koch, Z. Mamiyev, C. Tegenkamp, and H. Pfnür, *Thickness-dependent electronic transport through epitaxial nontrivial* Bi *quantum films*, Phys. Rev. B **102**, 115409 (2020).

[75] Z. Zhu, B. Fauqué, K. Behnia, and Y. Fuseya, *Magnetoresistance and valley degree of freedom in bulk bismuth*, J. Phys. Condens. Matter **30**, 313001 (2018).

[76] S. Zhang, Q. Wu, Y. Liu, and O. V. Yazyev, *Magnetoresistance from Fermi surface topology*, Phys. Rev. B **99**, 035142 (2019).

[77] S. Zhang, Z. Liu, H. Pi, Z. Fang, H. Weng, and Q. Wu, *Complex field-, temperature-, and angle-dependent Hall effects from intrinsic Fermi surface revealed by first-principles calculations*, Phys. Rev. B **110**, 205132 (2024).

[78] M. N. Ali *et al.*, *Large, non-saturating magnetoresistance in* WTe_2, Nature (London) **514**, 205 (2014).

[79] A. B. Pippard, *Magnetoresistance in Metals* (Cambridge University Press, Cambridge, England, 1989).

[80] M. Aitani, T. Hirahara, S. Ichinokura, M. Hanaduka, D. Shin, and S. Hasegawa, *In situ Magnetotransport measurements in ultrathin* Bi *films: Evidence for surface-bulk coherent transport*, Phys. Rev. Lett. **113**, 206802 (2014).

[81] G. M. Minkov, O. E. Rut, A. A. Sherstobitov, S. A. Dvoretski, N. N. Mikhailov, and A. V. Germanenko, *Quantum oscillations of transport coefficients and capacitance: A manifestation of the spin Hall effect*, Phys. Rev. B **108**, 075301 (2023).

[82] S. Datta, *Electronic Transport in Mesoscopic Systems* (Cambridge University Press, Cambridge, England, 1997).

[83] L. Onsager, *Interpretation of the de Haas-van Alphen effect*, London Edinburgh Dublin Phil. Mag. J. Sci. **43**, 1006 (1952).

[84] L. Li *et al.*, *Quantum oscillations in a two-dimensional electron gas in black phosphorus thin films*, Nat. Nanotechnol. **10**, 608 (2015).

[85] P. Streda, *Theory of quantised Hall conductivity in two dimensions*, J. Phys. C **15**, L717 (1982).

[86] V. Pudalov, S. Semenchinskii, and V. Edel'man, *Oscillations of the chemical potential and the energy spectrum of electrons in the inversion layer at a silicon surface in a magnetic field*, Sov. Phys. JETP **62**, 1079 (1985), http://jetp.ras.ru/cgi-bin/dn/e_062_05_1079.pdf.

[87] C. H. W. Barnes, D. R. Mace, G. Faini, D. Mailly, M. Y. Simmons, C. J. B. Ford, and M. Pepper, *Detection of the oscillation of the Fermi energy of a 2DEG*, Surf. Sci. **361–362**, 608 (1996).

[88] A. G. Davies, C. H. W. Barnes, K. R. Zolleis, J. T. Nicholls, M. Y. Simmons, and D. A. Ritchie, *Hybridization of single- and double-layer behavior in a double-quantum-well structure*, Phys. Rev. B **54**, R17331 (1996).

[89] C. Ellenberger, B. Simovič, R. Leturcq, T. Ihn, S. E. Ulloa, K. Ensslin, D. C. Driscoll, and A. C. Gossard, *Two-subband quantum Hall effect in parabolic quantum wells*, Phys. Rev. B **74**, 195313 (2006).

[90] C. A. Duarte, G. M. Gusev, A. A. Quivy, T. E. Lamas, A. K. Bakarov, and J. C. Portal, *Landau-level crossing in two-subband systems in a tilted magnetic field*, Phys. Rev. B **76**, 075346 (2007).

[91] M. Karalic, C. Mittag, S. Mueller, T. Tschirky, W. Wegscheider, K. Ensslin, T. Ihn, and L. Glazman, *Phase slips and parity jumps in quantum oscillations of inverted* InAs/GaSb *quantum wells*, Phys. Rev. B **99**, 201402 (2019).

[92] J. Ziegler, D. A. Kozlov, N. N. Mikhailov, S. Dvoretsky, and D. Weiss, *Quantum Hall effect and Landau levels in the three-dimensional topological insulator* HgTe, Phys. Rev. Res. **2**, 033003 (2020).

[93] https://cstr.cn/31125.02.SHMFF.HM.

[94] F. F. Fang and P. J. Stiles, *Effects of a tilted magnetic field on a two-dimensional electron gas*, Phys. Rev. **174**, 823 (1968).

[95] James G. Analytis, R. D. McDonald, S. C. Riggs, J.-H. Chu, G. S. Boebinger, and I. R. Fisher, *Two-dimensional surface state in the quantum limit of a topological insulator*, Nat. Phys. **6**, 960 (2010).

[96] S. Xu *et al.*, *Odd-integer quantum Hall states and giant spin susceptibility in p-type few-layer* WSe_2, Phys. Rev. Lett. **118**, 067702 (2017).

[97] G. E. Smith, G. A. Baraff, and J. M. Rowell, *Effective g factor of electrons and holes in bismuth*, Phys. Rev. **135**, A1118 (1964).

[98] R. D. Brown, *Shubnikov-de Haas measurements in bismuth*, Phys. Rev. B **2**, 928 (1970).

[99] Y. Liu and R. E. Allen, *Electronic structure of the semimetals* Bi *and* Sb, Phys. Rev. B **52**, 1566 (1995).

[100] J. M. Schneider, B. A. Piot, I. Sheikin, and D. K. Maude, *Using the de Haas–van Alphen effect to map out the closed three-dimensional Fermi surface of natural graphite*, Phys. Rev. Lett. **108**, 117401 (2012).

[101] B. Fallahazad, H. C. P. Movva, K. Kim, S. Larentis, T. Taniguchi, K. Watanabe, S. K. Banerjee, and E. Tutuc, *Shubnikov-de Haas oscillations of high-mobility holes in monolayer and bilayer* WSe_2*: Landau level degeneracy, effective mass, and negative compressibility*, Phys. Rev. Lett. **116**, 086601 (2016).

[102] G. Kresse and J. Furthmüller, *Efficient iterative schemes for ab initio total-energy calculations using a plane-wave basis set*, Phys. Rev. B **54**, 11169 (1996).

[103] P. E. Blöchl, *Projector augmented-wave method*, Phys. Rev. B **50**, 17953 (1994).

[104] J. P. Perdew, K. Burke, and M. Ernzerhof, *Generalized gradient approximation made simple*, Phys. Rev. Lett. **77**, 3865 (1996).

[105] S. Grimme, J. Antony, S. Ehrlich, and H. Krieg, *A consistent and accurate ab initio parametrization of density functional dispersion correction (DFT-D) for the 94 elements* H – Pu, J. Chem. Phys. **132**, 154104 (2010).